Vacuum 238 (2025) 114310

Contents lists available at ScienceDirect

Vacuum

journal homepage: www.elsevier.com/locate/vacuum

Boron depth distribution in iron surfaces at high-dose implantation

Z.T. Gaál [a,b,*], Z. Halász [b], A. Csík [b], V. Takáts [b], G. Nagy [c], J. Oscarsson [c], M. Sortica [c], D. Primetzhofer [c], T. Fodor [b], S. Molnár [b], J. Hakl [b], Zs Benkó [b], L. Daróczi [d], M. Benke [e], K. Vad [b], I. Rajta [b]

[a] University of Debrecen, Doctoral School of Physics, Debrecen, Hungary
[b] HUN-REN ATOMKI, Debrecen, Hungary
[c] Uppsala University, Uppsala, Sweden
[d] University of Debrecen, Department of Solid State Physics, Debrecen, Hungary
[e] University of Miskolc, Miskolc, Hungary

ARTICLE INFO

Handling Editor: Prof. L.G. Hultman

Keywords:
Implantation
Boron ions
High-dose implantation

ABSTRACT

Due to application of lead-free materials in soldering technology, the degradation of industrial tools is accelerated. However, this can be circumvented with boriding. Two types of boride phases are usually formed (FeB and Fe_2B), causing internal stress due to the different crystal structures. Our aim with B^+ ion implantations is to avoid this weakness and create a single-phase iron boride layer. The ion implantation was performed at different doses ($6.9{\cdot}10^{17}$–$1{\cdot}10^{18}$ ions/cm^2) of boron ions and with bombarding energies of 25 keV and 100 keV. The depth distribution of implanted boron was investigated by Secondary Neutral Mass Spectrometry (SNMS) depth profile analyses, Scanning Electron Microscopy (SEM) measurements, and by Elastic Recoil Detection Analysis (ERDA). The purpose of these measurements was to obtain information about the boron distribution produced by high-dose implantation. Our experimental analyses show that the boron distribution is more of a Pearson IV type than a Gaussian type.

1. Introduction

A common engineering challenge is to enhance the mechanical stability of surfaces while minimally altering the properties of the deeper underlying material, for example, hardening the surface while not changing the plasticity of the bulk material. Therefore, techniques were created focusing on the near-surface layers. Some of these methods, often called annealing, solely modify the crystal structure, whereas others introduce additional material, resulting in structural changes (referred to as surface alloying) [1].

Surface alloys can improve the mechanical properties of steels exposed to high temperatures [2–5]. A typical industrial application is in soldering technology: high temperatures required for proper solder handling can degrade nozzles of soldering tools, softening or even sealing them, rendering them useless. Studies have shown that the application of boron for surface modification can significantly extend the lifespan of nozzles, but the effectiveness depends greatly on the composition of the produced boride layers [6–11]. Two chemically distinct alloys are usually formed on the surface, FeB and Fe_2B, which are capable of achieving the desired technological effect [12–17]. However, they usually appear together, and their crystal structures are incompatible with each other. FeB features an orthorhombic crystal structure, whereas Fe_2B is tetragonal. When both are found in a sample surface, mechanical stress is induced at the interface between the two layers resulting in surface instability and peeling. This issue can be solved by forming only Fe_2B, which is compatible with the crystal structure of steel. The traditional method of surface boriding is the thermochemical surface treatment: boron atoms diffuse into iron by thermal excitation [18]. This procedure results in a boron-rich layer near the surface, making the presence of FeB inevitable and creating the desired composition mainly in the subsurface region of the material.

It is known for decades that amorphous phase is formed in crystalline metal substrates due to implantation [19–21]. Wilson et al. [22] suggested that Pearson IV distribution represents the depth profile of implanted ions for high-dose implantations, when the peak of ion distribution is broader and less sharp than a Gaussian curve.

The purpose of this work is to clarify the dose-dependent evolution of the emerging distribution of the boron ions in a bulk, high purity iron

* Corresponding author. University of Debrecen, Doctoral School of Physics, Debrecen, Hungary.
E-mail address: gaal.zoltan.tamas@atomki.hu (Z.T. Gaál).

https://doi.org/10.1016/j.vacuum.2025.114310
Received 17 February 2025; Received in revised form 1 April 2025; Accepted 2 April 2025
Available online 3 April 2025

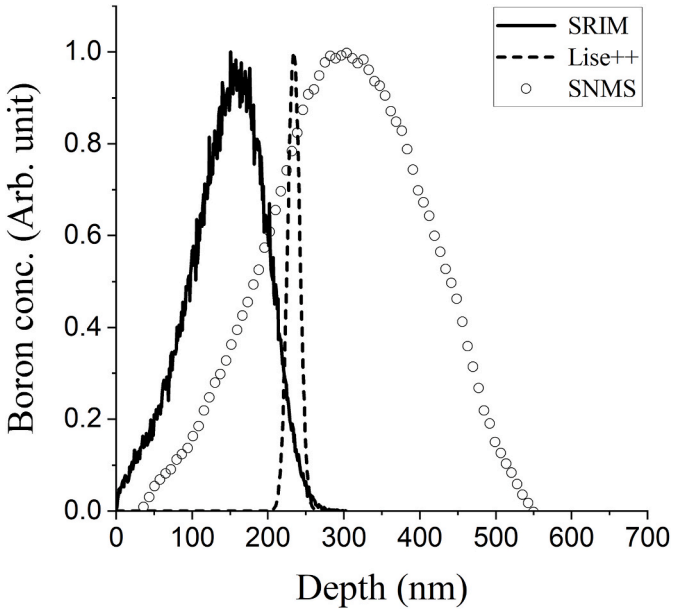

Fig. 1. SRIM simulation, LISE++ calculations and SNMS data of 100 keV B^+ ions range in iron target.

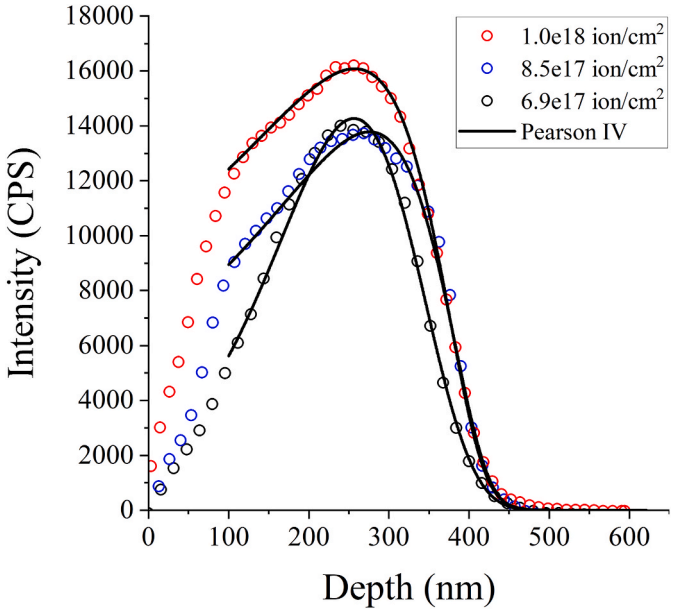

Fig. 2. SNMS depth profiles of iron implanted with 100 keV B^+ at doses of $6.9{\cdot}10^{17}$, $8.5{\cdot}10^{17}$ and $1.0{\cdot}10^{18}$ ions/cm^2 doses.

matrix.

2. Experimental details

For our experiments, 1 mm thick iron (GoodFellow FE000410/35) samples were prepared by cutting them into 1 cm^2 pieces. The pieces were mounted on an aluminum cylinder with polyvinyl acetate (PVA) for grinding each of them to the same plane. Then they were embedded in vinyl and polished to 11 nm average surface roughness with diamond suspension. In this way the thickness of the samples decreased to between 600 μm and 800 μm. The iron samples were implanted with boron ions while keeping them below 60 °C by water cooling to limit thermal diffusion during sample preparation. The implantations were performed with ion energies of 25 keV and 100 keV and doses of $6.9{\cdot}10^{17}$ to $1{\cdot}10^{18}$ ions/cm^2 using the implanter at Uppsala University [23]. These energies were chosen after SRIM (Stopping and Range of Ions in Matter) [24] simulations and LISE++ (Ligne d'Ions Super Epluchés, Super Peeled Ion Line) [25] calculations. We chose these two energies because with 25 keV the distribution of the stopped ions will be on the surface and with 100 keV it will start near the surface. With the increasing dose we assumed that the shape of the distribution would change and move toward the surface.

Both LISE++ and SRIM simulations provided us prediction of the range and the straggling of the ion penetration. Using these values, we could create an expected distribution of the boron ions as a function of the implantation dose. The range (mode of the distribution) predicted by SRIM in the target for the 100 keV boron ions was 144 nm, while the straggling was 50 nm (see Fig. 1). LISE calculated 234 nm for the range and 8 nm for the straggling. Our preliminary implantations on higher energies showed that the straggling given by SRIM was closer to the experiment while LISE predicted the range more accurately.

After implantation the boron depth distribution was studied by Secondary Neutral Mass Spectrometry (SNMS, type INA-X, SPECS GmbH) by using low-energy Ar^+ ions (E = 350 eV) in direct bombardment mode. Neutral particles sputtered by the Ar^+ ions were analyzed by a quadruple mass spectrometer (Balzers QMA 410) after post-ionization. The sputtered area was defined by circle shape Ta mask with 3 mm inner diameter. The lateral homogeneity of the ion bombardment and the depths of the sputtered craters were checked by a profilometer (Ambios XP-1). The boron depth distribution was also analyzed by Time-of-Flight Elastic Recoil Detection Analysis method (ToF-ERDA) employing 36 MeV I^{8+} primary ions using a 5 MV Pelletron tandem accelerator. Details of the set-up and evaluation procedure are found elsewhere [26]. Scanning Electron Microscopy (SEM) was performed with a JEOL JSM-IT500HR microscope using both secondary electron detector (SED) and backscattered electron detector (BED) at 15 kV accelerating voltage.

3. Results and discussion

Fig. 2 shows the boron distributions in iron samples implanted by 100 keV kinetic energy with $6.9{\cdot}10^{17}$, $8.5{\cdot}10^{17}$ and $1.0{\cdot}10^{18}$ ions/cm^2 doses. The resulting craters were used to calibrate the depth axis after the SNMS measurements using a profilometer, with an uncertainty of approximately 18 nm. As it can be seen, a shoulder begins to appear in the boron distribution near the surface as the implanted dose is increased. The origin of this phenomenon is that in case of high-dose implantation bombarding B^+ ions not only interact with iron atoms, but as the irradiation time increases, more and more boron is implanted interstitially, causing a gradual increase in stopping power, and the Bragg peak is shifted towards the surface. The intensity of the shoulder increases with the implanted dose, while the median of the respective distributions shifts towards the surface. Due to the asymmetry of the distribution, the SNMS data could not be properly fitted with a Gaussian curve. A Pearson IV distribution resulted in good fits below the appearing shoulder. The boron distribution between the surface and the shoulder remains approximately Gaussian.

Fig. 3 shows the ToF-ERDA and SNMS results of a 25 keV, $6.9{\cdot}10^{17}$ ions/cm^2 dose sample. The ToF-ERDA measurement shows a concentration depth profile that is in good agreement with the SNMS results. This agreement supports our conclusion that the decrease in the iron signal in the SNMS profiles is indeed due to lower iron concentrations in the implanted layer (also see Fig. 5a) and not the result of different sputtering or post-ionization properties. The boron ions implanted in high doses oversaturate the existing crystal structure, destroying the order and creating a disordered iron boride amorphous phase. The specific volume of this phase is greater than that of the packed structure, resulting in an apparent stretching of the material. This decrease in density is a result of the addition of lighter particles, the material becomes more packed with time. These investigations showed that the ions penetrated much deeper (the stopping range is approximately 125 nm

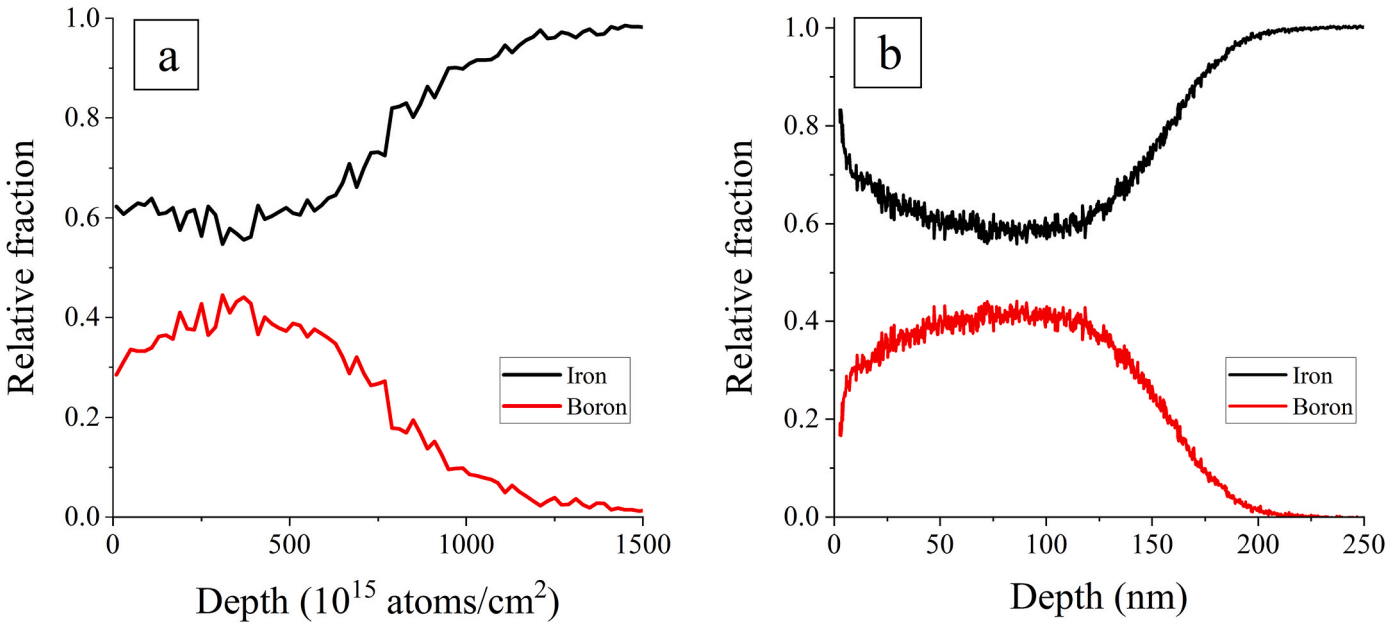

Fig. 3. Part a) ToF-ERDA and b) SNMS results of 25 keV B^+ ions implanted iron sample with $6.9{\cdot}10^{17}$ ions/cm^2 dose.

for 25 keV and 250–300 nm for 100 keV) and had a wider spread (FWHM >185 nm for 25 keV, >230 nm for 100 keV) than in the SRIM simulations.

Fig. 4 shows SEM images of the cross-section of an iron sample implanted with 25 keV B^+ ions. Due to the narrow iron boride layer in the sample, grinding and polishing was done at ~5° angle, rather than at the usual 90° angle, with the aim of better visualization of the iron boride structure in the microscope. Due to the 5° tilt angle, the 200 nm wide iron boride layer should appear to be about 2 μm wide. Since iron boride is much harder than high-purity iron and resin, it was ground more slowly, which apparently widened it to about 13.3 μm (with 0.8 μm uncertainty). We also investigated a non-implanted sample, where only the resin and the iron were visible. On the irradiated sample, however, the three distinct areas corresponding to resin, iron boride and iron were clearly separated. Due to the atomic number dependence of the sensitivity of the electron microscope, the resin (containing mostly H, O, C) appears in the image as a darker area while the iron boride and the iron appear as lighter grey areas. The boride layer also appears as a physical protrusion detectable by profilometer (shown in Part c), proving that its hardness has increased.

Due to implantation the iron matrix expands and becomes disordered, therefore the depth distribution of the iron atoms is not homogeneous. The inhomogeneity of iron atoms inside the implanted layer can be characterized by boron/iron vs. boron phase diagram obtained from SNMS measurements. Fig. 5a shows this phase diagram on a log-log scale for the sample implanted with 25 keV B^+ ions. The curve shows hysteresis-like behavior which can be caused by the increase in the boron concentration near the surface with a 'negative' Pearson (in the sense that the function is multiplied by minus one) iron distribution. The arising asymmetric distributions can still be evoked by the heat distribution along the depth during the deceleration of B^+ ions, and by an asymmetric matrix relaxation to the momentary peak of boron. Due to the depth distribution of the energy loss (Bragg curve), the local temperature is higher on the side of the distribution near to the surface.

Experimental data near the surface of the sample start at the boron/iron ratio of 0.3. The maximum of the ratio B/Fe can be found in a deeper layer of the sample. This part is called the increasing section. Moving further inside the sample, the B/Fe value decreases. This decreasing section can be divided into two parts. The first one appears to be linear; the second one varies as a polynomial. The highest value of the linear part indicates the location of the phase boundary between crystalline iron (original structure of the sample) and amorphous iron/iron-boride systems. On the SNMS diagram, this point corresponds to the point of the range where the iron signal reaches its maximum value (Fig. 5a). In order to test the expected behavior of the B/Fe ratio for different scenarios, we simulated the boron and iron distributions with calculated Pearson IV functions (which have a statistic, $\sqrt{n}$ uncertainty) for the following cases. The results and the way the boron/iron hysteresis curve changes depending on the relative position of the curves are shown on Fig. 5b–e. If the two distributions mirror each other (i.e. their extrema points are at the same depth), the boron/iron diagram appear as a single line (Fig. 5b) and the hysteresis disappears. If the two distributions are off-center compared to each other (Fig. 5c), or asymmetric distributions are centrally located compared to each other (Fig. 5d), the hysteresis character appears. In reality, both effects are present at the same time (Fig. 5e). Asymmetry can also refer to amorphization and bond rearrangement. As a consequence, the off-center character of the two distributions is the result of the iron matrix elongation in the sample. The curve can be fitted with a linear function at the end of the decreasing section of the boron distribution. This fit is possible because the B^+ ions did not stretch the iron matrix in the deeper part of the samples and a major part of the crystal structure remained intact locally.

If we investigate the widening and offset of the B/Fe – B curve in the phase space, we can see that the appearance of the hysteresis character is strongly influenced by the offset. On the other hand, the broadening of the Fe distribution retains the character of running together with less hysteresis but depends on the two branches belonging to the distributions. We showed with our experiments and simulations, that the B/Fe – B curve can be used to categorize the behaviors/changes of the implanted material and its matrix as a result of implantation. In our present case, the results show that the B and Fe distribution are not only asymmetric but also off-center. The reason for this behavior is the amorphization and bond rearrangement of the matrix.

4. Conclusions

In this study we determined the range distribution of implanted B^+ ions in high purity iron at high doses, which follows a Pearson IV type

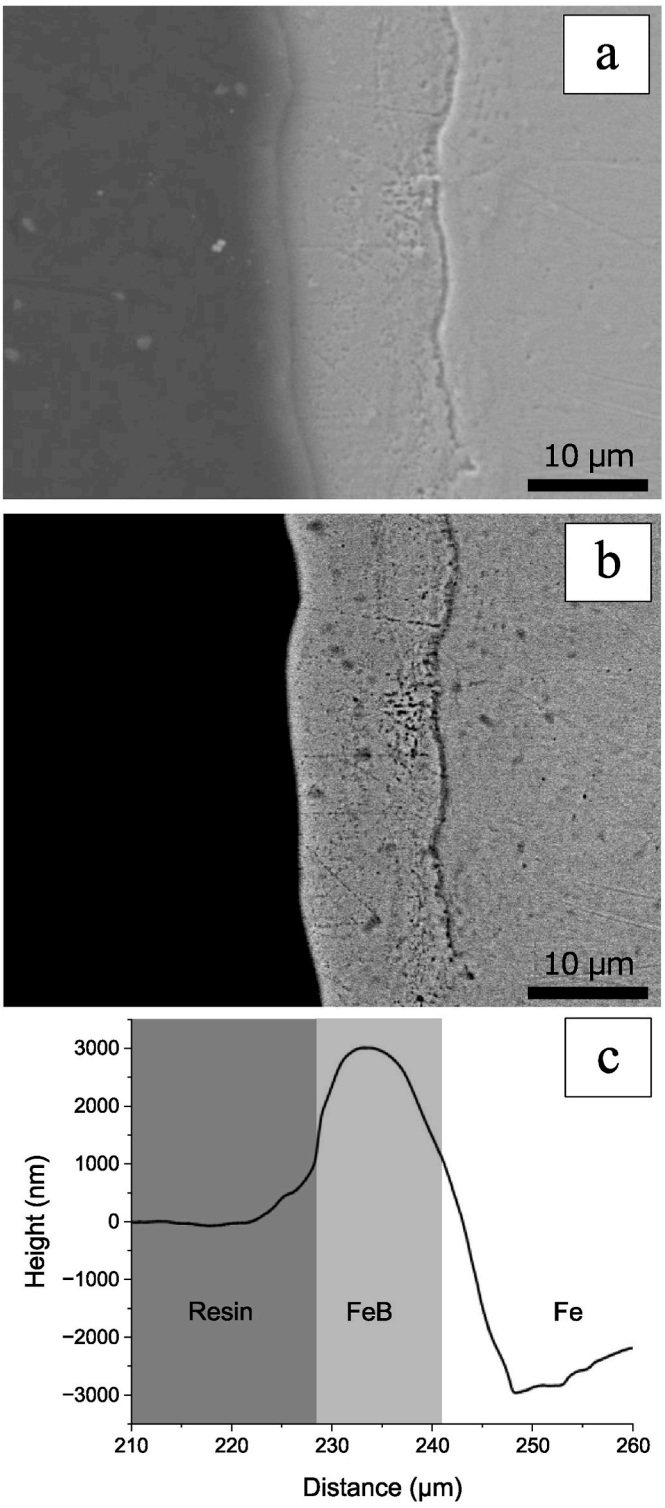

Fig. 4. Cross-section of an iron sample implanted with 25 keV boron ions. SEM images a) SED mode and b) BED mode. Part c) shows the result of the profilometer measurement.

distribution rather than a normal distribution. Furthermore, the distribution became wider and could be described by a more complicated function depending on the dose and energy. The SNMS measurements show that the boron ions penetrate deeper into the material than predicted by SRIM simulations and LISE++ calculations. The cause of these changes is that the increasing amount of stopped ions alters the matrix as the implantation proceeds, leading to a marked difference compared to low-dose implantation. The minimum of the iron distribution and the maximum of the depth distribution of boron atoms are not at the same depth (offset) and the amount of broadening of the distributions is different.

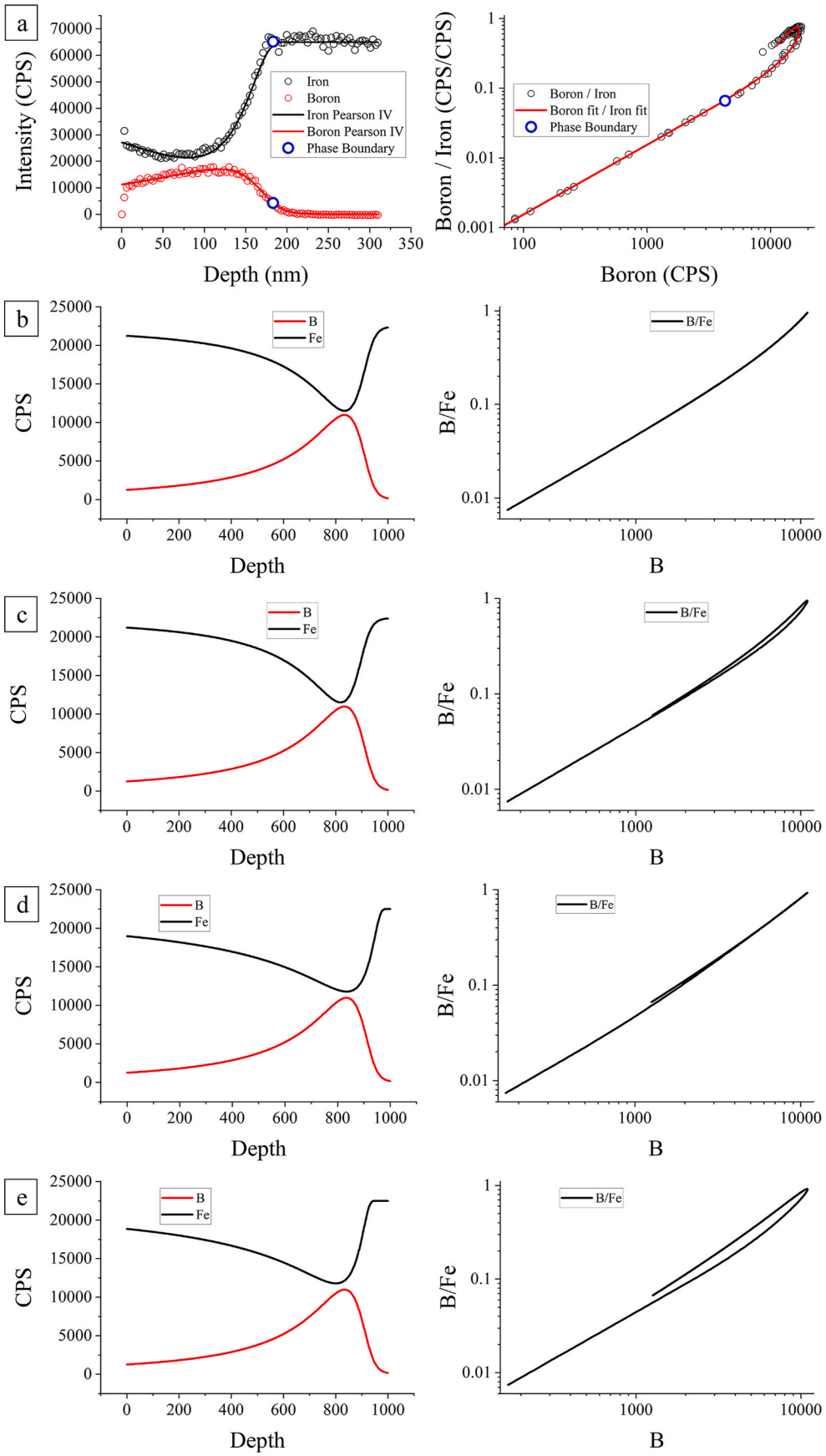

Fig. 5. Part a) Boron distribution in the boron/iron (boron) distributions phase plane of 25 keV boron implanted iron. Parts b-e) Simulation of the behavior of the boron/iron hysteresis curve depending on the position of the distributions.

CRediT authorship contribution statement

Z.T. Gaál: Writing – original draft, Visualization, Validation, Methodology, Investigation, Formal analysis, Data curation, Conceptualization. **Z. Halász:** Writing – review & editing, Methodology, Formal analysis, Data curation, Conceptualization. **A. Csík:** Writing – review & editing, Validation, Methodology, Investigation, Formal analysis. **V. Takáts:** Writing – review & editing, Methodology, Conceptualization. **G. Nagy:** Writing – review & editing, Validation, Investigation, Formal analysis, Data curation. **J. Oscarsson:** Validation, Formal analysis. **M. Sortica:** Validation, Formal analysis. **D. Primetzhofer:** Writing – review & editing, Project administration. **T. Fodor:** Writing – review & editing, Validation, Investigation, Formal analysis, Data curation. **S. Molnár:** Writing – review & editing, Investigation, Formal analysis. **J. Hakl:** Writing – review & editing, Methodology, Formal analysis, Conceptualization. **Zs Benkó:** Methodology, Formal analysis. **L. Daróczi:** Methodology, Formal analysis. **M. Benke:** Writing – review & editing, Methodology, Conceptualization. **K. Vad:** Writing – review & editing, Supervision, Methodology, Conceptualization. **I. Rajta:** Writing – review & editing, Supervision, Methodology, Conceptualization.

Declaration of competing interest

The authors declare that they have no known competing financial interests or personal relationships that could have appeared to influence the work reported in this paper.

Acknowledgements

This work was supported by the RADIATE project under Grant Agreement No. 824096 from the EU Research and Innovation Programme HORIZON 2020 and by the project TKP2021-NKTA-42 financed by the National Research, Development and Innovation Fund of the Ministry for Innovation and Technology, Hungary. Accelerator operation at Uppsala University was supported by the Swedish research Council VR-RFI (contract #2019_00191).

Data availability

Data will be made available on request.

References

[1] Michal Kulka, Current Trend in Boriding, Engineering Materials, Springer, Cham, 2019, https://doi.org/10.1007/978-3-030-06782-3.
[2] S. Sen, I. Ozbek, U. Sen, C. Bindal, Mechanical behavior of borides formed on borided cold work tool steel, Surf. Coating. Technol. 135 (2001) 173–177, https://doi.org/10.1016/S0257-8972(00)01064-1.
[3] E. Atik, U. Yunker, C. Meric, The effects of conventional heat treatment and boronizing on abrasive wear and corrosion of SAE 1010, SAE 1040, D2 and 304 steels, Tribol. Int. 36 (2003) 155–161, https://doi.org/10.1016/S0301-679X(02)00069-5.
[4] I. Uslu, H. Comert, M. Ipek, F.G. Celebi, O. Ozdemir, C. Bindal, A comparison of borides formed on AISI 1040 and AISI P20 steels, Mater. Des. 28 (2007) 1819–1826, https://doi.org/10.1016/j.matdes.2006.04.019.
[5] M. Erdoğan, I. Gunes, A. Dalar, Investigation of corrosion behavior of borided gear steels, Trans. Indian Inst. Met. 67 (2013) 291–297, https://doi.org/10.1007/s12666-013-0329-8.
[6] Z. Salyi, G. Kaptay, D. Koncz-Horvath, et al., Boride coatings on steel protecting it against corrosion by a liquid lead-free solder alloy, Metall. Mater. Trans. B 53 (2022) 730–743, https://doi.org/10.1007/s11663-021-02412-2.
[7] H. Nishikawa, T. Takemoto, K. Kifune, T. Uetani, N. Sekimori, Effect of iron plating conditions on reaction in molten lead-free solder, Mater. Trans. 45 (2004) 741–746, https://doi.org/10.2320/matertrans.45.741.
[8] T. Takemoto, T. Uetani, M. Yamazaki, Dissolution rates of iron plating on soldering iron tips in molten lead-free solders Sold, Surf. Mount. Technol. 16 (2004) 9–15, https://doi.org/10.1108/09540910410562473.
[9] Y.C. Huang, et al., Dissolution and interfacial reactions of Fe in molten Sn-Cu and Sn-Pb solders, J. Mater. Res. 22 (2007) 2924–2929, https://doi.org/10.1557/JMR.2007.0361.
[10] T. Ishida, The reaction of solid iron with molten tin, Trans. JIM. 14 (1973) 37–44, https://doi.org/10.2320/matertrans1960.14.37.
[11] A.N. Campbell, J.H. Wood, G.B. Skinner, The system iron—tin: liquidus only, J. Am. Chem. Soc. 71 (1949) 1729–1733, https://doi.org/10.1021/ja01173a052.
[12] I. Campos-Silva, M. Ortiz-Domínguez, H. Cimenoglu, R. Escobar-Galindo, M. Keddam, M. Elías-Espinosa, N. López-Perrusquia, Diffusion model for growth of Fe_2B layer in pure iron, Surf. Eng. 27 (2011) 189–195, https://doi.org/10.1179/026708410X12550773057820.
[13] M. Keddama, Z. Nait Abdellah, M. Kulkac, R. Chegrounea, Determination of the diffusion coefficients of boron in the FeB and Fe_2B layers formed on AISI D2 steel, Acta Phys. Pol. Ser. a 128 (2015) 740–745, https://doi.org/10.12693/APhysPolA.128.740.
[14] R. Kouba, M. Keddam, M. Kulka, Modelling of paste boriding process, Surf. Eng. 31 (2015) 563–569, https://doi.org/10.1179/1743294414Y.0000000357.
[15] I. Campos-Silv, M. Flores-Jiménez, D. Bravo-Bárcenas, H. Balmori-Ramírez, J. Andraca-Adame, J. Martínez-Trinidad, J.A. Meda-Campaña, Evolution of boride layers during a diffusion annealing process, Surf. Coating. Technol. 309 (2017) 155–163, https://doi.org/10.1016/j.surfcoat.2016.11.054.
[16] M. Ipek, G. Celebi Efe, I. Ozbek, S. Zeytin, C. Bindal, Investigation of boronizing kinetics of AISI 51100 steel, J. Mater. Eng. Perform. 21 (2012) 733–738, https://doi.org/10.1007/s11665-012-0192-5.
[17] Y. Gencer, Indose of manganese on pack boriding behaviour of pure iron, Surf. Eng. 27 (2011) 634–638, https://doi.org/10.1179/1743294411Y.0000000010.
[18] M. Keddam, S.M. Chentouf, A diffusion model for describing the bilayer growth (FeB/Fe2B) during the iron powder-pack boriding, Appl. Surf. Sci. 252 (2005) 393–399, https://doi.org/10.1016/j.apsusc.2005.01.016.
[19] W.A. Grant, Ion-implantation and irradiation studies using amorphous metals, Nucl. Instrum. Methods 182–183 (1981) 809–826, https://doi.org/10.1016/0029-554x(81)90814-4.
[20] S. Prussin, D.I. Margolese, R.N. Tauber, Formation of amorphous layers by ion implantation, J. Appl. Phys. 57 (1985) 180–185, https://doi.org/10.1063/1.334840.
[21] K. Suzuki, K. Kawamura, Y. Kikuchi, Y. Kataoka, Compact model for amorphous layer thickness formed by ion implantation over wide ion implantation conditions, IEEE Trans. Electron. Dev. 53 (2006) 1186–1192, https://doi.org/10.1109/ted.2006.872695.
[22] Robert G. Wilson, The pearson IV distribution and its application to ion implanted depth profiles, Radiat. Eff. 46 (3–4) (1980) 141–147, https://doi.org/10.1080/00337578008209163.
[23] P. Ström, D. Primetzhofer, Ion beam tools for nondestructive in-situ and in-operando composition analysis and modification of materials at the Tandem Laboratory in Uppsala, J. Instrum. 17 (2022), https://doi.org/10.1088/1748-0221/17/04/P04011.
[24] James F. Ziegler, M.D. Ziegler, J.P. Biersack, SRIM – the stopping and range of ions in matter, Nucl. Instrum. Methods Phys. Res. Sect. B Beam Interact. Mater. Atoms 268 (2010) 1818–1823, https://doi.org/10.1016/j.nimb.2010.02.091.
[25] D. Bazin, O. Tarasov, M. Lewitowicz, O. Sorlin, The program LISE: a simulation of fragment separators, Nucl. Instrum. Methods A 482 (2002) 307–327, https://doi.org/10.1016/S0168-9002(01)01504-2.
[26] P. Ström, P. Petersson, M. Rubel, G. Possnert, A combined segmented anode gas ionization chamber and time-of-flight detector for heavy ion elastic recoil detection analysis, Rev. Sci. Instrum. 87 (2016) 103303, https://doi.org/10.1063/1.4963709.